Tip-induced superconductivity enhancement in single-crystalline PdSb by point-contact spectroscopy

Chufan Chen,[1,2] Dongting Zhang,[1,2] Rohit Kumar,[1,*] Yanan Zhang,[1,2] Ge Ye,[1,2] Lichang Yin,[1,2] Jiawen Zhang,[1,2] Huiqiu Yuan,[1,2,3,4] Chao Cao,[1,2,†] and Xin Lu[1,2,4,‡]

[1]*Center for Correlated Matter, School of Physics, Zhejiang University, Hangzhou 310058, China*
[2]*Zhejiang Province Key Laboratory of Quantum Technology and Device, Zhejiang University, Hangzhou 310027, China*
[3]*State Key Laboratory of Silicon Materials, Zhejiang University, Hangzhou 310027, China*
[4]*Collaborative Innovation Center of Advanced Microstructures, Nanjing University, Nanjing 210093, China*

(Received 28 April 2022; revised 4 October 2022; accepted 16 November 2022; published 30 November 2022)

We report our mechanical point-contact spectroscopy (MPCS) study on single-crystalline superconductor PdSb with $T_c \sim 1.32$ K and $\mu_0 H_{c2}(0) \sim 900$ Oe, whose T_c changes very slightly against hydrostatic pressure below 2.5 GPa. For MPCS with a soft Au tip, the Andreev reflection signals suggest the same superconducting temperature T_c as in the pristine PdSb crystal and the conductance curves show a fully gapped behavior, yielding a superconducting gap value of $\Delta_0 = 0.23$ meV with $2\Delta_0/k_B T_c \sim 4.25$ in the strong-coupling regime. However, for MPCS with a hard W tip, an enhanced superconducting T_c can be observed with a concomitant increase in the superconducting gap Δ in a linear relation of 0.109 meV/kelvin, whereas $2\Delta_0/k_B T_c$ decreases from 4.25 to 3.5 in a negative correlation with T_c. From first-principles calculations, we observe a Lifshitz transition related to Pd-4d_{z^2} orbitals under uniaxial pressure, which is absent under hydrostatic pressure. Such Lifshitz transition results in an enhanced density of states near the Fermi level $n(E_F)$, which is in line with the enhanced T_c. In addition, a soft phonon mode at H is hardened under uniaxial pressure, suggesting a reduced coupling strength in this case. Such local strain effect provides a natural explanation for our MPCS results on PdSb.

DOI: 10.1103/PhysRevB.106.174520

I. INTRODUCTION

Topological superconductors (TSC) have attracted intensive attention in recent years due to its exotic physical properties and possible application on fault-tolerant quantum computations [1–6]. One way to realize the TSC is to proximitize topological materials to a conventional *s*-wave superconductor (SC) in a heterostructure [7–10]. However, it requires detailed procedures for heterostructure growth to achieve a clean interface, and an alternative strategy is to search for intrinsic TSC by exploring nontrivial topological materials with intrinsic superconductivity, such as the nematic superconductors $Cu_xBi_2Se_3$, $PbTaSe_2$ [11–13], spin-triplet SC UTe_2 [14,15], and inducing SC in topological materials by tuning pressure or gate voltage [16–18]. Among them, point-contact spectroscopy (PCS) plays as a powerful tool to induce local SC by tip or epoxy on the sample surface, which has broadened the application of point-contact method [19,20]. For example, emergent SC has been reported by PCS on some topological materials, such as Cd_3As_2, TaAs, WC, ZrSiS, $NbAs_2$, and $TaAs_2$ [21–28]. Meanwhile, a local T_c enhancement has also been observed in recent PCS measurements on Au_2Pb, Sr_2RuO_4, and AV_3Sb_5 (A = K and Cs) [29–31]. Although the underlying mechanism is probably associated with a local pressure/strain or charge-transfer effect at the interface [32], it is still a challenge to ensure a ballistic contact to probe the superconducting order parameter due to the damaged tip geometry during tip engagement, and more careful experiments are required to explore topological materials, especially topological superconductors.

Recently, superconductors with the NiAs-type structure have triggered much interest in the community [33]. For example, superconductivity has been reported for PdSb ~ 1.5, PtSb ~ 2.1, PdBi ~ 1.21, and PdTe ~ 2.3 K [34], whereas little has been known on their superconducting properties. In particular, the T_c in single-crystalline PdTe has reached as high as 4.5 K, nearly twice than the previous study [35], and a strong-coupling behavior was observed from its heat-capacity measurement [36]. The significantly enhanced T_c supports the ability to synthesize high-quality crystals for the NiAs-type materials, which offers an ideal platform to investigate possible topological superconductors in the presence of heavy elements with a strong spin-orbit coupling.

In this article, we have successfully synthesized PdSb single crystals and applied mechanical PCS (MPCS) to probe its SC order parameter. PdSb crystals show a SC transition temperature $T_c \sim 1.32$ K, which changes little under hydrostatic pressure up to 2.5 GPa. For Au-tip MPCS, the differential conductance curves can be well fitted by a single-gap Blonder-Tinkham-Klapwijk (BTK) model [37] at 0.3 K and show a consistent T_c with the pristine sample. The superconducting gap Δ follows a typical Bardeen-Cooper-Schrieffer (BCS) temperature behavior, yielding $\Delta_0 = 0.23$ meV and $2\Delta_0/k_B T_c$

*Corresponding author: rohit@zju.edu.cn
†Corresponding author: ccao@zju.edu.cn
‡Corresponding author: xinluphy@zju.edu.cn

= 4.25 in the strong-coupling regime. In contrast, for the tungsten-tip MPCS, an enhanced local superconducting T_c can be observed as high as 2.4 K with a concomitant increase in the superconducting gap Δ. Combined with first-principles calculations, we argue that the T_c enhancement can be ascribed to the local strain effect from the hard tungsten tip.

II. METHODS

A. Experiment

PdSb single crystals (space-group $P6_3/mmc$, No. 194 [38]) were grown using Sb self-flux. Starting material comprising of Pd and Sb pieces in a 45:55 atomic ratio was loaded in an alumina crucible [39], capped with silica wool, and sealed under vacuum in a silica ampoule. The ampoule was placed in a programmable box furnace where the temperature was raised to 630 °C in 6 h and kept there for 2 h before further heating up the furnace to 950 °C in 15 h. Furnace temperature was maintained at 950 °C for 16 h, and then lowered to 800 °C in 5 h. The furnace was then slowly cooled to 730 °C in 100 h, at which point the ampoule was taken out of the furnace, inverted, and loaded into a centrifuge within 3 sec. Postcentrifugation, single crystals as big as $6 \times 6 \times 5$ mm^3 partly covered in solidified Sb were recovered from the crucible. The composition of the crystals was confirmed on an Oxford scanning electron microscope by carrying out energy dispersive x-ray spectroscopic measurements on the surface of polished crystals where data was collected over ten points on each crystal. The crystallinity of the single crystals was also confirmed by carrying out Laue diffraction on multiple crystals.

Electrical resistance was measured by the standard four-probe method, and the resistance measurement under pressure was carried out in a piston-cylinder-type pressure cell up to 2.5 GPa where Daphne 7373 oil was used as the pressure medium for good hydrostaticity. Mechanical PCS in a needle-anvil type was employed to study the superconducting gap in PdSb where a sharp gold or tungsten tip prepared by the elelctrochemical etching was engaged onto the polished *ab* plane of the sample by piezoelectric nanopositioners and to have current flowing in the directional *c* axis across the contact junction. The PCS differential conductance curve as a function of bias voltage $G(V)$ was recorded by the conventional lock-in technique in a quasi-four-probe configuration. Our PCS and electrical resistance measurements were accomplished in an Oxford cryostat with ^{3}He inserted down to 0.3 K and the maximum magnetic field can be 8 T. Meanwhile, the heat capacity of PdSb down to 0.4 K was measured in the physical property measurement system with a ^{3}He insert from Quantum Design.

B. First-principles calculations

The first-principles calculations were performed using plane-wave basis density functional theory (DFT) as implemented in Vienna *ab initio* simulation package [40]. The valence-ion interactions and exchange-correlation functional were approximated using projected augmented-wave method [41,42] and Perdew, Burke, and Ernzerhoff parametrization [43]. The plane-wave energy cut-off was set to be 480 eV as Pd-4*p* and Sb-4*d* orbitals were regarded as valence electrons in our calculations. A Γ-centered $12 \times 12 \times 9$ K mesh was used for the Brillioun zone integration in the self-consistent calculations, whereas a denser $24 \times 24 \times 16$ K mesh was used in the density of states (DOS) calculations. The above setting ensures the total energy converges to 1 meV/atom. The crystal structure under ambient and hydrostatic pressures were fully relaxed until forces on each atom was less than 1 meV/Å and internal stress less was than 1 kbar; whereas the crystal structure uniaxial pressure were obtained by fixing a reduced *c* lattice constant and relaxing the in-plane axis as well as the atomic coordinates. The phonon properties were calculated using density functional perturbation theory as implemented in the QUANTUM ESPRESSO package [44,45].

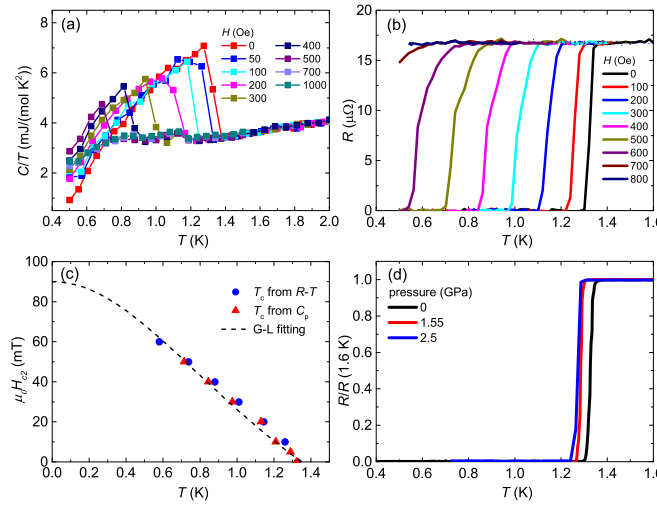

FIG. 1. The (a) temperature-dependent heat-capacity C/T and (b) electrical resistance R of the PdSb sample in different magnetic fields; (c) the upper critical field H_{c2} obtained from the specific heat and resistance on the H-T phase diagram with the dashed line from the G-L fitting; (d) Temperature dependence of electrical resistance of PdSb under different pressures.

III. RESULTS

Figures 1(a) and 1(b) show the temperature-dependent heat capacity (HC) and electrical resistance results on the freshly synthesized PdSb single crystals as a function of magnetic field. Both measurements evidence a sharp superconducting transition at 1.32 K in zero field, suggesting a high quality of our PbSb crystals. Superconductivity is gradually suppressed by the field and finally absent above 700 Oe for HC and 800 Oe for resistance measurements. The upper critical field $\mu_0 H_{c2}$ as a function of temperature has been constructed in the H-T phase diagram as in Fig. 1(c) based on the half transition of heat capacity and resistance results in Figs. 1(a) and 1(b), respectively, and they follow a consistent behavior in the Ginzburg-Landau formula as $\mu_0 H_{c2}(T) = \mu_0 H_{c2}(0)(1 - t^2)/(1 + t^2)$, where $t = T/T_c$ is the reduced temperature and the extrapolated $\mu_0 H_{c2}(0)$ is 900 Oe at 0 K. Since the $\mu_0 H_{c2}$ for PdSb is quite isotropic in different crystal orientations, we can estimate the coherence length $\xi_{\mathrm{GL}}(0) \sim 61$ nm from

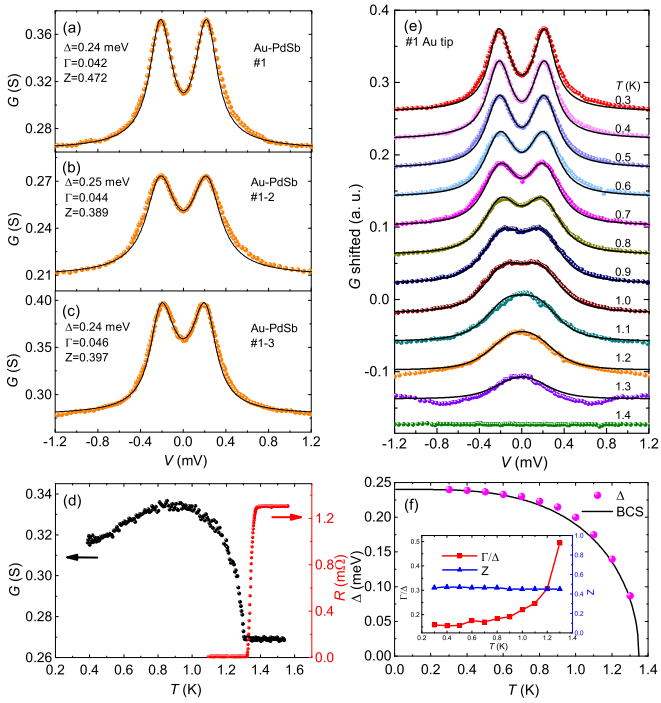

FIG. 2. (a)–(c) A representative set of differential conductance curves $G(V)$ from different point contacts on PdSb at 0.3 K, in comparison with an s-wave BTK fitting (black lines); (d) the zero-bias conductance G_0 as a function of temperature with a kink at 1.31 K, in comparison with the resistance data; (e) temperature evolution of differential conductance curves $G(V)$ from 0.3 to 1.4 K, in comparison with the s-wave BTK fitting (black lines). The curves are vertically shifted for clarity; (f) temperature dependence of the extracted superconducting gap Δ with the standard BCS curve (black line). The fitting parameters Z and Γ/Δ as functions of temperature are shown in the inset.

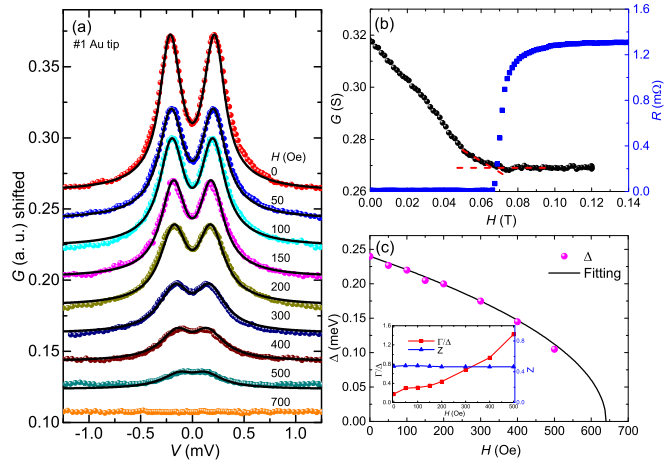

FIG. 3. (a) Differential conductance curves $G(V)$ of PdSb at 0.3 K under different magnetic fields, in comparison with the s-wave BTK fitting; (b) zero-bias conductance as a function of magnetic field at 0.3 K, in comparison with the magnetoresistance data in PdSb. The upper critical field of the ZBC is guided by the cross of two red dashed lines. (c) Field dependence of the extracted superconducting gap in accordance with $\Delta(H) = \Delta(0)\sqrt{1 - H/H_{c2}}$. The inset shows the fitting parameters Z and Γ/Δ as a function of field.

the formula $\xi_{GL}(0)=\{\phi_0/[2\pi\mu_0 H_{c2}(0)]\}^{1/2}$ with ϕ_0 as the magnetic flux quanta. Furthermore, we measured the PdSb electrical resistance under applied pressure up to 2.5 GPa as in Fig. 1(d), showing the superconducting T_c for PdSb only changes slightly against the hydrostatic pressure below 2.5 GPa.

For MPCS on PdSb with an Au tip, a representative set of differential conductance curves $G(V)$ for three different contacts are shown in Figs. 2(a)–2(c) with a common double-peak feature at 0.3 K. We note that the contact diameter can be estimated by the formula $a = \sqrt{\frac{4\rho l}{3\pi R_s}}$ in the assumption of ballistic contact. For the contact resistance in the range of 1–5 Ω, the contact diameter a is 3.6–8 nm, smaller than the mean free path $l \sim 13.4$ nm, consistent with the assumption of ballistic limit. Moreover, no obvious dip structure in the conductance curves can be observed at the lowest temperature, supporting the contacts in the ballistic regime. They can be well fitted by the single-gap s-wave BTK model, supporting a full superconducting gap Δ around 0.24 meV at 0.3 K. We note that the obtained smearing parameter Γ is in the range between 0.042 and 0.046 meV, indicating a small scattering rate and, thus, a clean interface in our case. A slight deviation can be noted at higher bias voltages in the $G(V)$ curves, but this should not compromise our BTK analysis. The temperature evolution of our point-contact conductance curves in comparison with the optimal s-wave BTK fitting curves are shown in Fig. 2(e) from 0.3 to 1.4 K where the double peaks are gradually suppressed into a zero-bias peak and the $G(V)$ finally becomes flat at 1.4 K in the normal state. If we track the point-contact conductance at zero-bias conductance (ZBC) as a function of temperature as in Fig. 2(d), a kink around 1.31 K signals the disappearance of Andreev reflection and a transition from superconducting to normal state in PdSb, consistent with the transition temperature determined by the heat capacity and resistance measurements. The extracted superconducting gap values Δ from BTK fitting are plotted in Fig. 2(f) as a function of temperature, and they follow a typical BCS temperature behavior, yielding $\Delta_0 \sim 0.24$ meV and $2\Delta_0/k_B T_c = 4.25$ for PdSb in the strong-coupling regime similar to Pb [46]. We note that the tunneling barrier parameter Z almost keeps constant with temperature, whereas the ratio between smearing parameter Γ and superconducting gap Δ, Γ/Δ, increases rapidly close to T_c as shown in the inset of Fig. 2(f), probably due to the enhanced pair-breaking effect [47].

Magnetic-field evolution of $G(V)$ curves for the Au tip on PdSb at 0.3 K are shown in Fig. 3(a) in comparison with the s-wave BTK fitting. The superconducting signal has been gradually suppressed with the field up to 700 Oe: The heights of double-peaks are reduced and the peak positions shift to zero-bias voltage until 700 Oe. To more accurately determine the upper critical field, we plot the zero-bias conductance curve as a function of field in Fig. 3(b). The kink around 650 Oe defines the $\mu_0 H_{c2}$ at 0.3 K, consistent with the magnetoresistance results as in Fig. 3(b). The extracted gap values as a function of field are shown in Fig. 3(c), complying with the typical type-II superconductor behavior

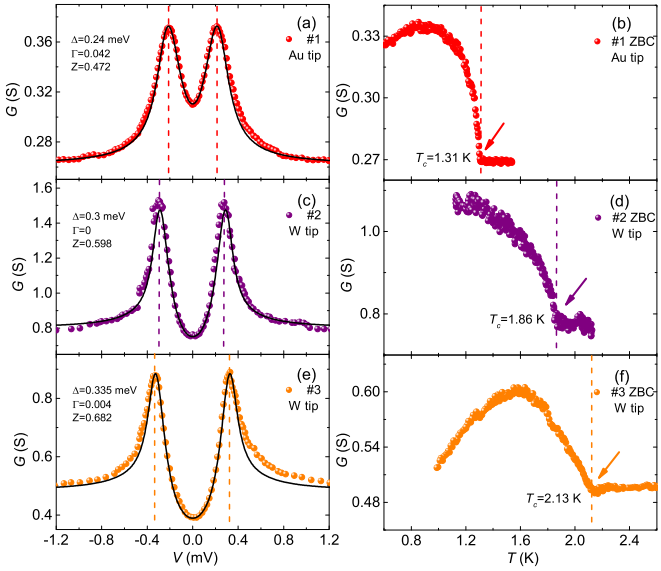

FIG. 4. Differential conductance curves from different contacts with (a) Au tip (No. 1) and (b) and (c) W tip (Nos. 2 and 3), (e) on PdSb at 0.3 K, in comparison with *s*-wave BTK fitting (black lines). The dashed lines are a guide to eyes to show the evolution of superconducting gap; (b), (d), and (f) zero-bias conductance curves as a function of temperature from the corresponding contacts in (a), (c), and (e), with dashed lines and arrows as a guide to the eyes for the local T_c.

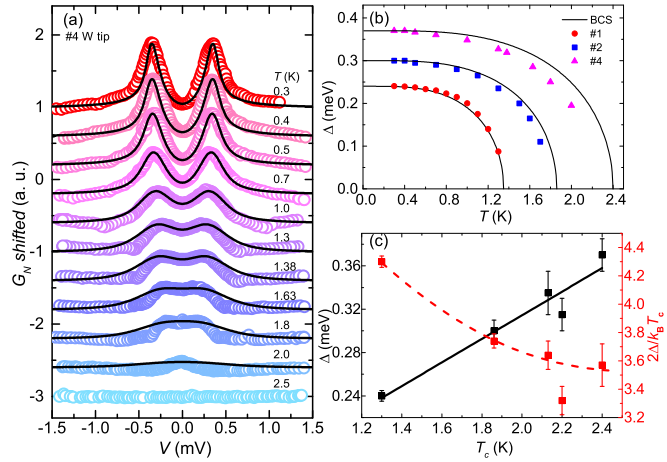

FIG. 5. (a) Temperature dependence of the differential conductance curves for point-contact between a W tip and a PdSb crystal, in comparison with the *s*-wave BTK fitting (black lines); (b) The extracted superconducting gap values as a function of temperature for contacts with Au (No. 1) and W (Nos. 2 and 4) tips, in comparison with their corresponding BCS curves; (c) the extracted superconducting gap values Δ_0 and the coupling parameter, $2\Delta_0/k_BT_c$ as a function of local transition temperature T_c in different PCS contacts. The solid and dashed lines are guides to the eyes.

with $\Delta(H) = \Delta(0)\sqrt{1 - H/H_{c2}}$. We note that the tunneling barrier parameter Z barely changes with the field, suggesting a stable contact for our PCS, whereas the ratio of smearing parameter and gap Γ/Δ increases as a function of magnetic field as in the inset of Fig. 3(c) due to the pair-breaking effect with more vortex in the contact region.

In order to make a comparison with the Au-tip PCS, the tungsten tip has been applied to make contact with PdSb crystals, whose hardness can generally induce a more obvious local pressure or strain effect on samples. In such a case, an enhanced local superconducting T_c and gap value have been observed for the W tip on PdSb as in Fig. 4. Figs. 4(a) and 4(b) show the differential conductance curve and zero-bias conductance, respectively, for the Au tip on PdSb as a reference where the superconducting T_c is the same as that from heat capacity and resistance measurements. In sharp contrast, for a W tip on PdSb, its zero-bias conductance curve in Fig. 4(d) shows an increased transition temperature T_c up to 1.86 K, much larger than the intrinsic bulk value, whereas the peak position in $G(V)$ shifts to a bigger value as shown in Fig. 4(c), and the extracted superconducting gap increases to 0.30 meV with the BTK fitting, nearly 30% bigger than the Au-tip case. Another contact with the W tip (No. 3) even exhibits a more dramatic enhancement of T_c up to 2.13 K and the superconducting gap increases up to 0.335 meV as in Figs. 4(e) and 4(f), showing a positive correlation between the superconducting gap and the local T_c. We note that the smearing parameter Γ for the W tip in the BTK analysis is small, signaling a very clean interface. The origin of the local enhanced superconductivity in the case of the W tip may be associated with the tip-induced strain effect on PdSb restricted in the contact area as discussed later.

Figure 5(a) shows the temperature-dependent $G(V)$ curves for W-tip PCS on the PdSb crystal in comparison with the optimal BTK fitting where the fitting parameters Z=0.532 and Γ=0.001 meV. The double peaks are gradually suppressed into a zero-bias peak and finally become flat at 2.5 K in the normal state. The zero-bias conductance curve as a function of temperature also identifies a local T_c of 2.4 K, nearly twice than the intrinsic $T_c \sim 1.32$ K, whereas the extracted superconducting gap Δ is enhanced to 0.37 meV. If we summarize the temperature dependence of superconducting gap values for contacts with both Au and W tips in Fig. 5(b), the gap well follows the BCS temperature curve for the case of the Au-tip No. 1 and the W-tip No. 2, whereas it shows a noticeable deviation in the W-tip No. 4 case. This may be caused by the obvious dip structure at higher bias voltages in W-tip No. 4 PCS at high temperatures due to the heating effect in the the contact area, which results in a systematical underestimate of the superconducting gap values. Even though the superconducting gap Δ increases with the enhanced local T_c in a positive linear correlation of 0.109 meV/kelvin as plotted in Fig. 5(c), $2\Delta/k_BT_c$ decreases instead from 4.25 (in the strong-coupling regime) to the weak-coupling limit 3.5, probably associated with an evolution of the electron-phonon coupling strength under strain.

In order to understand the experimental observations, we have also performed first-principles calculations for PdSb at ambient pressure, hydrostatic pressure at 2 GPa, and uniaxial pressure at 1.8 GPa, respectively. We compile the relaxed crystal lattice constants and atomic coordinates in Table I. At the ambient pressure, the fully relaxed lattice constants are $a = 4.1445$ Å and $c/a = 1.3743$. The calculated

TABLE I. Lattice constants from first-principles calculations under different pressures. 2^h denotes hydrostatic 2-GPa pressure, and 1.8^u denotes uniaxial 1.8-GPa pressure. x_{Pd} and x_{Sb} are the coordinates of Wyckoff positions of Pd and Sb atoms, respectively.

	a (Å)	c/a	x_{Pd}	x_{Sb}
0 GPa	4.1445	1.3743		
2^h GPa	4.1193	1.3741	(0, 0, 1/2)	(1/3, 2/3, 3/4)
1.8^u GPa	4.1699	1.3420		

a value is slightly larger than the experimental observation (4.076 Å [38]) but within 2% error bar of the well-known overestimation of bond lengths in GGA calculations. The c/a ratio is also in consistency with the experimental value of 1.3722. These results show the validity of the chosen exchange-correlation functional, and suggest that the system is most likely weakly correlated. Under 2-GPa hydrostatic pressure, a shrinks to 4.1193 Å whereas the c/a ratio is 1.3741, nearly unchanged. In contrast, uniaxial 1.8-GPa pressure along the c axis reduces the c/a ratio to 1.3420.

In Fig. 6, we show the electronic band-structure results. In all cases, the electronic states near the Fermi level are dominated by the Pd-4d and Sb-5p orbitals as also confirmed in the DOS calculations (Fig. 7). At ambient pressure as well as hydrostatic 2-GPa pressure, there are three doubly degenerate bands crossing the Fermi level, giving rise to three Fermi surfaces. We must point out that the hydrostatic pressure has a negligible effect on the electronic band structure except for the effect of slightly increased reciprocal lattice lengths. For example, the highest occupied state at Γ, which is mainly contributed by the Pd-d_{z^2} orbitals, are 0.12 and 0.125 eV below the Fermi level at ambient pressure and hydrostatic 2 GPa, respectively. In fact, if we normalize the reciprocal lattice constants, the band energy shifts between $E_F \pm 1.0$ eV are all within 10 meV. As a result, the DOS at the Fermi level $n(E_F)$ changes only ∼1%, from 0.915 eV^{-1}/f.u. at the ambient pressureto 0.903 eV^{-1}/f.u. at hydrostatic 2 GPa. The $n(E_F)$ value at the ambient pressure corresponds to $\gamma_0 = 2.16$ mJ mol^{-1} K^{-2}. This is comparable to the experimental value of $\gamma = 2.63$ mJ mol^{-1} K^{-2}, in consistency with our argument that the compound is weakly correlated.

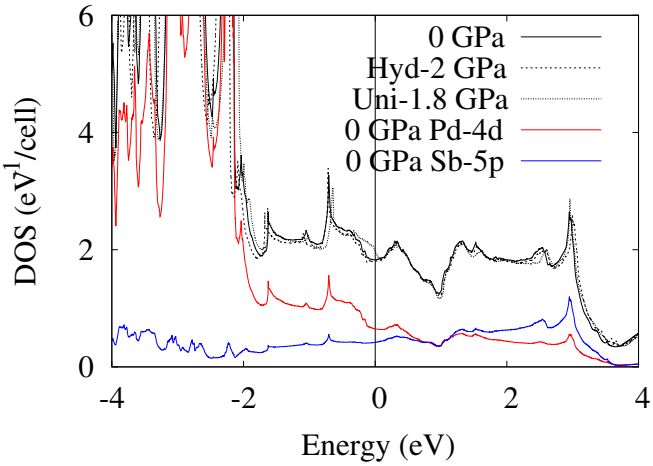

FIG. 7. The DOS of PdSb. The solid black line is the total DOS at ambient pressure; the dashed black line is the total DOS at hydrostatic 2 GPa; the dotted black line is the total DOS at uniaxial 1.8 GPa; the solid red line is the the projected DOS of Pd-4d orbitals at ambient pressure; the solid blue line is the projected DOS of Sb-5p orbitals at ambient pressure.

The situation is dramatically different if uniaxial pressure is applied. In this case, the energy of the above-mentioned Pd-d_{z^2} state at Γ is significantly enhanced. At around 1.8-GPa uniaxial pressure, a Lifshitz transition occurs as a result, creating a fourth doubly degenerate hole pocket sheet. This, in turn, leads to an enhancement of $n(E_F)$ at 0.987 eV^{-1}/f.u. (Fig. 7). In fact, $n(E_F)$ at 3.5-GPa uniaxial pressure turns out to be 1.06 eV^{-1}/f.u., nearly 16% enhanced compared to the ambient pressure value.

It is also instructive to examine the phonon band structure of PdSb (Fig. 8). The hexagonal lattice is stable in all three cases as the phonon spectra are stable. Therefore, no structural phase transition is related with the experimental observations. It is worthy noting that the phonon band 7/8 has a substantial V-shaped dip around H at ambient pressure. Such a soft phonon mode may be related with enhanced electron-phonon coupling at H. This mode is less affected by the hydrostatic pressure as it is also present in the hydrostatic 2-GPa calculation. However, in the uniaxial 1.8-GPa

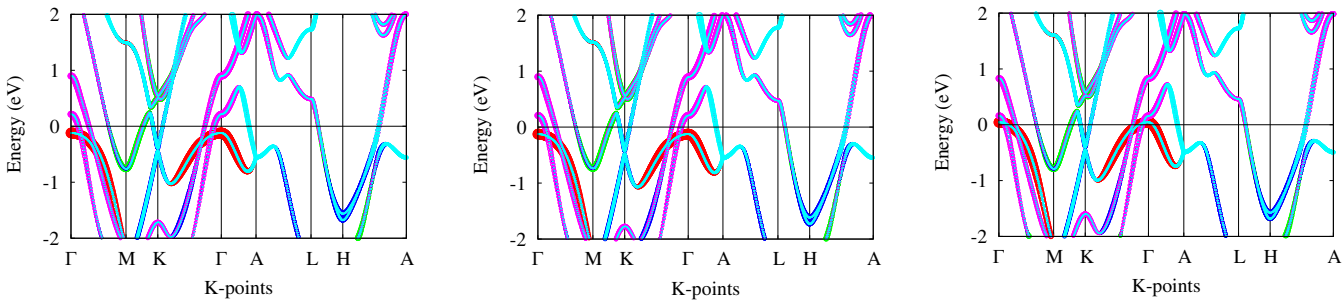

(a) 0 GPa (b) Hydrostatic 2 GPa (c) Uniaxial 1.8 GPa

FIG. 6. Electronic band structure of PdSb at (a) ambient pressure, (b) 2-GPa hydrostatic pressure, and (c) 1.8-GPa uniaxial pressure on the c axis. The radii of red, green, blue, cyan, and magenta circles are proportional to orbital contributions of Pd-d_{z^2}, Pd-d_{zx}/d_{zy}, Pd-$d_{x^2-y^2}/d_{xy}$, Sb-p_z, and Sb-p_x/p_y. The Fermi levels are aligned to 0 in all panels.

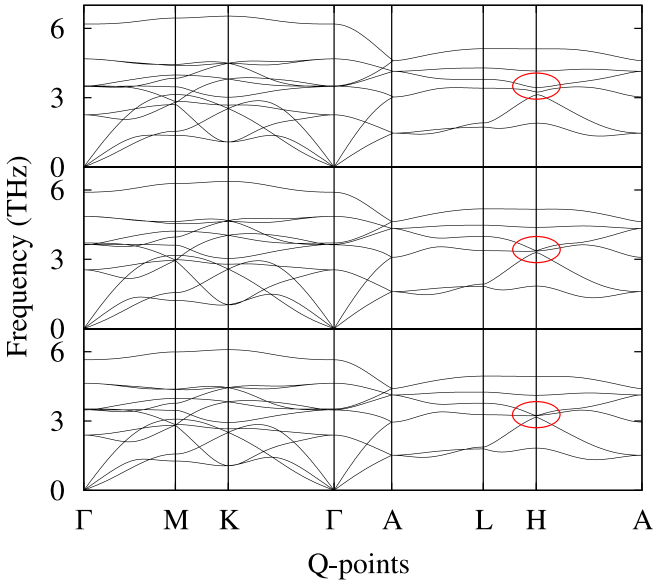

FIG. 8. Phonon band structure of PdSb. From bottom to top panels: ambient pressure, hydrostatic 2 GPa, and uniaxial 1.8 GPa. The soft phonon mode at H around 3 THz is highlighted in red circles.

calculation, the V-shaped dip is suppressed, suggesting a reduction of electron-phonon coupling at H.

IV. DISCUSSION AND CONCLUSION

First, we would discuss the possible origin of the tip-enhanced superconductivity in PdSb: In general, the tip-induced superconductivity (TISC) or tip-enhanced superconductivity (TESC) for PCS is caused by the local pressure/strain or charge-transfer effect at the interface of the contact region [20,32]. We can probably exclude the scenario of the charge-transfer effect in our measurement since a noticeable tip-induced TISC or TESC effect should also be expected for the Au-tip case similar to the triple-point semimetal WC [26]. However, our Au-tip PCS has probed the intrinsic T_c in the PdSb sample instead. On the other hand, we cannot simply attribute the TESC in PdSb to a local tip-pressure effect where only a small decrease in superconducting T_c has been observed under hydrostatic pressure up to 2.5 GPa as shown in Fig. 1(d). In fact, our DFT calculations also suggest negligible variation of electronic DOS at the Fermi level and phonon spectra under hydrostatic pressure. We would, thus, argue the local strain may tune the superconducting state in the contact area where the hard W tip achieves a compressive strain only in the c direction on PdSb and, thus, yields a local T_c enhancement. DFT calculations suggest it most likely to be a result of Lifshitz transition from uniaxial pressure, leading to a substantially enhanced $n(E_F)$ compared to the ambient pressure case. We note the Au tip sometimes can cause a slight superconducting trace below 1.76 K besides a dominant contribution from the intrinsic superconductivity below 1.32 K, and the enhanced T_c is much lower than that of the W tip. It is probably caused by the nonuniform strain effect with the softer Au tip compared with the hard W tip. Uniaxial strain measurements on PdSb would be helpful to finally address the origin of the enhanced superconducting T_c.

Second, we focus on the issue of decreasing superconducting parameter $2\Delta_0/k_BT_c$ in the presence of the tip-induced strain effect. For PdSb, the intrinsic $2\Delta_0/k_BT_c$ is 4.25 in the strong-coupling regime. Its T_c can be determined by McMillan's equation [48], $T_c = \frac{\Theta_D}{1.45}\exp[\frac{-1.04(1+\lambda)}{\lambda-\mu^*(1+0.62\lambda)}]$, where Θ_D is the Debye temperature, μ^* is the effective electron-electron repulsion term, and λ is the electron-phonon coupling term. Here, $\lambda = 2\int_0^\infty \frac{\alpha^2(\omega)F(\omega)}{\omega}d\omega$, $\alpha^2(\omega)$ is the coupling strength between the electron and the phonon with frequency ω, and $F(\omega)$ is the phonon density of states. In calculations, it is observed that a soft phonon mode exists at ~3 THz at H under both ambient and hydrostatic pressures. Usually, such a soft phonon mode is related with highly anisotropic electron-phonon coupling, and should, thus, be strongly coupled. In the case of W-tip PCS, the decreased $2\Delta_0/k_BT_c$ may suggest a reduced λ for electron-phonon coupling, and we speculate it arises from phonon hardening and reduced $\alpha^2(\omega)$ under local strain [49]. This is also supported by our DFT calculations, which show a suppression of the soft phonon mode at H under uniaxial pressure. On the other hand, increased Debye temperature may compensate it, and the aforementioned Lifshitz transition-induced $n(E_F)$ increases further enhances the superconducting T_c instead. We note, in some nanoparticles, the enhanced superconducting coupling parameter originates from the increased surface to volume ratio where surface phonons are softer than bulk [46].

In conclusion, we have grown PdSb single crystals and characterized their superconducting gaps by point-contact spectroscopy with both Au and W tips. Our results can be summarized as follows: (1) PdSb single crystals show a superconducting transition temperature of 1.32 K with an upper critical field $\mu_0H_{c2}(0) \sim 900$ Oe, both in the heat-capacity and electrical resistance measurements, whereas its superconductivity changes slightly against hydrostatic pressure below 2.5 GPa. (2) PCS with an Au tip shows a fully gapped behavior where the gap $\Delta_0 \sim 0.23$ meV with $2\Delta_0/k_BT_c \sim 4.25$ in the strong-coupling regime, and it follows a type-II superconductor behavior in the magnetic field. (3) PCS with a hard W tip shows an enhanced local T_c with an concomitant increase in the superconducting gap Δ, probably due to the local strain effect applied by the hard tip. However, we have observed a decrease in $2\Delta_0/k_BT_c$ with enhanced T_c. First-principles calculations show a Lifshitz transition and hardening of a soft phonon mode at H under uniaxial pressure, absent under hydrostatic pressure, which may result in an enhanced density of states near the Fermi level $n(E_F)$ and enhanced superconductivity. Our results show that PCS is a powerful tool to tune the superconductivity and induce TESC, and further uniaxial strain studies would be called for to further explore the associated mechanism of enhanced T_c in PdSb.

ACKNOWLEDGMENTS

The work at Zhejiang University was supported by the National Key R&D Program of China (Grants No. 2022YFA1402200 and No. 2017YFA0303100), the National Natural Science Foundation of China (Grants No. 12174333

and No. 11874137), and the Key R&D Program of Zhejiang Province, China (Grant No. 2021C01002). X.L. would like to acknowledge support from the Zhejiang Provincial Natural Science Foundation of China (Grant No. LR18A040001).

[1] C. Beenakker and L. Kouwenhoven, A road to reality with topological superconductors, Nat. Phys. **12**, 618 (2016).
[2] F. Wilczek, Majorana returns, Nat. Phys. **5**, 614 (2009).
[3] C. Nayak, S. H. Simon, A. Stern, M. Freedman, and S. Das Sarma, Non-abelian anyons and topological quantum computation, Rev. Mod. Phys. **80**, 1083 (2008).
[4] M. Sato, Topological properties of spin-triplet superconductors and Fermi surface topology in the normal state, Phys. Rev. B **79**, 214526 (2009).
[5] M. Sato and Y. Ando, Topological superconductors: A review, Rep. Prog. Phys. **80**, 076501 (2017).
[6] X.-L. Qi, T. L. Hughes, S. Raghu, and S.-C. Zhang, Time-Reversal-Invariant Topological Superconductors and Superfluids in Two and Three Dimensions, Phys. Rev. Lett. **102**, 187001 (2009).
[7] L. Fu and C. L. Kane, Superconducting Proximity Effect and Majorana Fermions at the Surface of a Topological Insulator, Phys. Rev. Lett. **100**, 096407 (2008).
[8] J.-P. Xu, M.-X. Wang, Z. L. Liu, J.-F. Ge, X. Yang, C. Liu, Z. A. Xu, D. Guan, C. L. Gao, D. Qian, Y. Liu, Q.-H. Wang, F.-C. Zhang, Q.-K. Xue, and J.-F. Jia, Experimental Detection of a Majorana Mode in the core of a Magnetic Vortex inside a Topological Insulator-Superconductor $Bi_2Te_3/NbSe_2$ heterostructure, Phys. Rev. Lett. **114**, 017001 (2015).
[9] M.-X. Wang, C. Liu, J.-P. Xu, F. Yang, L. Miao, M.-Y. Yao, C. L. Gao, C. Shen, X. Ma, X. Chen, Z.-A. Xu, Y. Liu, S.-C. Zhang, D. Qian, J.-F. Jia, and Q.-K. Xue, The coexistence of superconductivity and topological order in the Bi_2Se_3 thin films, Science **336**, 52 (2012).
[10] E. Wang, H. Ding, A. V. Fedorov, W. Yao, Z. Li, Y.-F. Lv, K. Zhao, L.-G. Zhang, Z. Xu, J. Schneeloch, R. Zhong, S.-H. Ji, L. Wang, K. He, X. Ma, G. Gu, H. Yao, Q.-K. Xue, and S. Chen, Xi and Zhou, Fully gapped topological surface states in Bi_2Se_3 films induced by a d-wave high-temperature superconductor, Nat. Phys. **9**, 621 (2013).
[11] K. Matano, M. Kriener, K. Segawa, Y. Ando, and G.-q. Zheng, Spin-rotation symmetry breaking in the superconducting state of $Cu_xBi_2Se_3$, Nat. Phys. **12**, 852 (2016).
[12] S. Yonezawa, K. Tajiri, S. Nakata, Y. Nagai, Z. Wang, K. Segawa, Y. Ando, and Y. Maeno, Thermodynamic evidence for nematic superconductivity in $Cu_xBi_2Se_3$, Nat. Phys. **13**, 123 (2017).
[13] T. Le, Y. Sun, H.-K. Jin, L. Che, L. Yin, J. Li, G. Pang, C. Xu, L. Zhao, S. Kittaka, T. Sakakibara, K. Machida, R. Sankar, H. Yuan, G. Chen, X. Xu, S. Li, Y. Zhou, and X. Lu, Evidence for nematic superconductivity of topological surface states in $PbTaSe_2$, Sci. Bull. **65**, 1349 (2020).
[14] S. Ran, C. Eckberg, Q.-P. Ding, Y. Furukawa, T. Metz, S. R. Saha, I.-L. Liu, M. Zic, H. Kim, J. Paglione, and N. P. Butch, Nearly ferromagnetic spin-triplet superconductivity, Science **365**, 684 (2019).
[15] L. Jiao, S. Howard, S. Ran, Z. Wang, J. O. Rodriguez, M. Sigrist, Z. Wang, N. P. Butch, and V. Madhavan, Chiral superconductivity in heavy-fermion metal UTe_2, Nature (London) **579**, 523 (2020).
[16] K. Kirshenbaum, P. S. Syers, A. P. Hope, N. P. Butch, J. R. Jeffries, S. T. Weir, J. J. Hamlin, M. B. Maple, Y. K. Vohra, and J. Paglione, Pressure-Induced Unconventional Superconducting Phase in the Topological Insulator Bi_2Se_3, Phys. Rev. Lett. **111**, 087001 (2013).
[17] C. Zhang, L. Sun, Z. Chen, X. Zhou, Q. Wu, W. Yi, J. Guo, X. Dong, and Z. Zhao, Phase diagram of a pressure-induced superconducting state and its relation to the Hall coefficient of Bi_2Te_3 single crystals, Phys. Rev. B **83**, 140504(R) (2011).
[18] E. Sajadi, T. Palomaki, Z. Fei, W. Zhao, P. Bement, C. Olsen, S. Luescher, X. Xu, J. A. Folk, and D. H. Cobden, Gate-induced superconductivity in a monolayer topological insulator, Science **362**, 922 (2018).
[19] S. Howlader and G. Sheet, Tip-induced superconductivity, J. Phys.: Condens. Matter **33**, 403002 (2021).
[20] H. Wang, L. Ma, and J. Wang, Tip-induced or enhanced superconductivity: a way to detect topological superconductivity, Sci. Bull. **63**, 1141 (2018).
[21] H. Wang, H. Wang, H. Liu, H. Lu, W. Yang, S. Jia, X.-J. Liu, X. C. Xie, J. Wei, and J. Wang, Observation of superconductivity induced by a point contact on 3D Dirac semimetal Cd_3As_2 crystals, Nature Mater. **15**, 38 (2016).
[22] L. Aggarwal, A. Gaurav, G. S. Thakur, Z. Haque, A. K. Ganguli, and G. Sheet, Unconventional superconductivity at mesoscopic point contacts on the 3D Dirac semimetal Cd_3As_2, Nature Mater. **15**, 32 (2016).
[23] H. Wang, H. Wang, Y. Chen, J. Luo, Z. Yuan, J. Liu, Y. Wang, S. Jia, X.-J. Liu, J. Wei, and J. Wang, Discovery of tip induced unconventional superconductivity on Weyl semimetal, Sci. Bull. **62**, 425 (2017).
[24] X.-Y. Hou, Y.-D. Gu, S.-J. Li, L.-X. Zhao, W.-L. Zhu, Z. Wang, M.-D. Zhang, F. Zhang, L. Zhang, H. Zi, Y.-W. Wu, H.-X. Yang, Z.-A. Ren, P. Zhang, G.-F. Chen, N. Hao, and L. Shan, Two superconducting phases induced at point contacts on the Weyl semimetal TaAs, Phys. Rev. B **101**, 134503 (2020).
[25] L. Aggarwal, S. Gayen, S. Das, R. Kumar, V. Süß, C. Felser, C. Shekhar, and G. Sheet, Mesoscopic superconductivity and high spin polarization coexisting at metallic point contacts on Weyl semimetal TaAs, Nat. Commun. **8**, 13974 (2017).
[26] X.-y. Hou, Z. Wang, Y.-d. Gu, J.-b. He, D. Chen, W.-l. Zhu, M.-d. Zhang, F. Zhang, Y.-f. Xu, S. Zhang, H.-x. Yang, Z.-a. Ren, H.-m. Weng, N. Hao, W.-g. Lv, J.-p. Hu, G.-f. Chen, and L. Shan, Superconductivity induced at a point contact on the topological semimetal tungsten carbide, Phys. Rev. B **100**, 235109 (2019).
[27] L. Aggarwal, C. K. Singh, M. Aslam, R. Singha, A. Pariari, S. Gayen, M. Kabir, P. Mandal, and G. Sheet, Tip-induced superconductivity coexisting with preserved topological properties in line-nodal semimetal ZrSiS, J. Phys.: Condens. Matter **31**, 485707 (2019).
[28] M.-D. Zhang, X.-Y. Hou, Q. Wang, Y.-Y. Wang, L.-X. Zhao, Z. Wang, Y.-D. Gu, F. Zhang, T.-L. Xia, Z.-A. Ren, G.-F. Chen,

N. Hao, and L. Shan, Tip-induced superconductivity on the topological semimetals $TaAs_2$ and $NbAs_2$, Phys. Rev. B **102**, 085139 (2020).

[29] Y. Xing, H. Wang, C.-K. Li, X. Zhang, J. Liu, Y. Zhang, J. Luo, Z. Wang, Y. Wang, L. Ling, M. Tian, S. Jia, J. Feng, X.-J. Liu, J. Wei, and J. Wang, Superconductivity in topologically nontrivial material Au_2Pb, npj Quantum Mater. **1**, 16005 (2016).

[30] H. Wang, W. Lou, J. Luo, J. Wei, Y. Liu, J. E. Ortmann, and Z. Q. Mao, Enhanced superconductivity at the interface of W/Sr_2RuO_4 point contacts, Phys. Rev. B **91**, 184514 (2015).

[31] L. Yin, D. Zhang, C. Chen, G. Ye, F. Yu, B. R. Ortiz, S. Luo, W. Duan, H. Su, J. Ying, S. D. Wilson, X. Chen, H. Yuan, Y. Song, and X. Lu, Strain-sensitive superconductivity in the kagome metals KV_3Sb_5 and CsV_3Sb_5 probed by point-contact spectroscopy, Phys. Rev. B **104**, 174507 (2021).

[32] W. Zhu, X. Hou, J. Li, Y. Huang, S. Zhang, J. He, D. Chen, Y. Wang, Q. Dong, M. Zhang, H. Yang, Z. Ren, J. Hu, L. Shan, and G. Chen, Interfacial superconductivity on the topological semimetal tungsten carbide induced by metal deposition, Adv. Mater. **32**, 1907970 (2020).

[33] B. T. Matthias, Superconducting compounds of nonsuperconducting elements, Phys. Rev. **90**, 487 (1953).

[34] T. H. Geballe, B. T. Matthias, B. Caroli, E. Corenzwit, J. P. Maita, and G. W. Hull, 3*d* Elements in superconducting PdSb, Phys. Rev. **169**, 457 (1968).

[35] B. Tiwari, R. Goyal, R. Jha, A. Dixit, and V. P. S. Awana, PdTe: a 4.5 K type-II BCS superconductor, Supercond. Sci. Technol. **28**, 055008 (2015).

[36] A. B. Karki, D. A. Browne, S. Stadler, J. Li, and R. Jin, PdTe: A strongly coupled superconductor, J. Phys.: Condens. Matter **24**, 055701 (2012).

[37] G. E. Blonder, M. Tinkham, and T. M. Klapwijk, Transition from metallic to tunneling regimes in superconducting microconstrictions: Excess current, charge imbalance, and supercurrent conversion, Phys. Rev. B **25**, 4515 (1982).

[38] J. N. Pratt, K. M. Myles, J. B. Darby, Jr., and M. H. Mueller, X-ray studies of palladium-cadmium and palladium-antimony alloys, J. Less-Common Met. **14**, 427 (1968).

[39] Pd-Sb Binary Phase Diagram 0-100 at. % Sb.

[40] G. Kresse and J. Hafner, *Ab initio* molecular dynamics for liquid metals, Phys. Rev. B **47**, 558 (1993).

[41] G. Kresse and D. Joubert, From ultrasoft pseudopotentials to the projector augmented-wave method, Phys. Rev. B **59**, 1758 (1999).

[42] P. E. Blöchl, Projector augmented-wave method, Phys. Rev. B **50**, 17953 (1994).

[43] J. P. Perdew, K. Burke, and M. Ernzerhof, Generalized Gradient Approximation Made Simple, Phys. Rev. Lett. **77**, 3865 (1996).

[44] P. Giannozzi, S. Baroni, N. Bonini *et al.*, Quantum espresso: A modular and open-source software project for quantum simulations of materials, J. Phys.: Condens. Matter **21**, 395502 (2009).

[45] F. Giustino, Electron-phonon interactions from first principles, Rev. Mod. Phys. **89**, 015003 (2017).

[46] S. Bose, C. Galande, S. P. Chockalingam, R. Banerjee, P. Raychaudhuri, and P. Ayyub, Competing effects of surface phonon softening and quantum size effects on the superconducting properties of nanostructured Pb, J. Phys.: Condens. Matter **21**, 205702 (2009).

[47] D. Daghero and R. S. Gonnelli, Probing multiband superconductivity by point-contact spectroscopy, Supercond. Sci. Technol. **23**, 043001 (2010).

[48] W. L. McMillan, Transition temperature of strong-coupled superconductors, Phys. Rev. **167**, 331 (1968).

[49] M. Kakihana, M. Osada, M. Käll, L. Börjesson, H. Mazaki, H. Yasuoka, M. Yashima, and M. Yoshimura, Raman-active phonons in $Bi_2Sr_2Ca_{1-x}Y_xCu_2O_{8+d}$ (x=0–1): Effects of hole filling and internal pressure induced by Y doping for Ca, and implications for phonon assignments, Phys. Rev. B **53**, 11796 (1996).